



Cite this: *RSC Adv.*, 2017, 7, 21214

# Fabrication of TiO<sub>2</sub> coated porous CoMn<sub>2</sub>O<sub>4</sub> submicrospheres for advanced lithium-ion anodes

 Jun Zhou,<sup>a</sup> Shuang Cheng,<sup>a</sup>  <sup>\*,a</sup> Yu Jiang,<sup>a</sup> Fenghua Zheng,<sup>a</sup> Xing Ou,<sup>a</sup> Lufeng Yang,<sup>a</sup> Mengkun Wang,<sup>a</sup> Minghai Yao<sup>a</sup> and Meilin Liu  <sup>\*,ab</sup>

Herein, a facile and general way for the synthesis of TiO<sub>2</sub> coated cobalt manganese oxide CoMn<sub>2</sub>O<sub>4</sub> (CMO) has been developed. In this contribution, uniform Co<sub>0.33</sub>Mn<sub>0.67</sub>CO<sub>3</sub> spheres are firstly fabricated via a solvothermal method. Porous CMO with a diameter of about 800 nm is obtained by a subsequent annealing procedure. Finally, a thin layer of TiO<sub>2</sub> is coated on the surface of the CMO through a hydrolysis and subsequent condensation process. When evaluated as anode materials for lithium ion batteries (LIBs), after 500 cycles at a current density of 1000 mA g<sup>-1</sup>, the CMO@TiO<sub>2</sub> spheres possessed high reversible capacities of 940 mA h g<sup>-1</sup> with a suitable discharge plateau of ~0.6 V, much higher than the pristine CMO. In addition, the CMO@TiO<sub>2</sub> shows better rate performance than CMO, as high as 196 mA h g<sup>-1</sup> at a very fast discharge current of 5 A g<sup>-1</sup>. The high electrochemical performance of CMO@TiO<sub>2</sub> should be attributed to its special structure of nanometer scale spheres with high porosity and the thin layer coating of TiO<sub>2</sub> as a zero-strain shell, which can effectively reduce the diffusion length of electrolyte, Li<sup>+</sup> and electrons, buffer volume expansion during the Li<sup>+</sup> insertion/extraction processes and thus reduce the materials' pulverization.

Received 7th March 2017

Accepted 6th April 2017

DOI: 10.1039/c7ra02789c

rsc.li/rsc-advances

## 1. Introduction

Lithium ion batteries (LIBs) have become one of the most important power sources for portable devices, electric vehicles and energy storage power stations nowadays, but the development of advanced batteries with higher energy density and power density within a certain weight or volume is still a challenge. As an indispensable part of LIBs, anode materials play a key role in improving the performance of batteries and have always been a focus of the energy storage area. Up to now, carbon materials and Li<sub>4</sub>Ti<sub>5</sub>O<sub>12</sub> are the two commonly used commercial anode materials, and Si-based anode materials are regarded as most commercial potential materials for next generation LIBs.<sup>1–3</sup> Transition metal oxides (TMOs), such as Co<sub>3</sub>O<sub>4</sub>,<sup>4–6</sup> Mn<sub>3</sub>O<sub>4</sub>,<sup>7,8</sup> Fe<sub>2</sub>O<sub>3</sub>,<sup>9,10</sup> and NiO<sup>11</sup> also have long been reckoned as potential anode materials for LIBs due to their many attractive features, including high theoretical capacities, high power density and environmental benign. However, these materials inevitably suffer from several major problems: severe volume changes during charge–discharge processes, agglomeration and pulverization of particles, and poor electronic conductivity.<sup>12</sup> New research is constantly being carried out to

meet the increasing requirements for LIBs anodes. In recent years, mixed transition metal oxides (MTMOs) have been attracting great research interest as anodes in LIBs owing to their outstanding features:<sup>13</sup> (1) synergistic effect, attributed to different expansion coefficients of two types of metal elements; (2) higher reversible capacities, due to its complex chemical compositions which can alloy with more Li ions compared with normal metal oxides;<sup>14</sup> (3) higher electrical conductivity, owing to relatively low activation energy; (4) more environmental benign. A promising family of MTMOs is A<sub>x</sub>B<sub>3–x</sub>O<sub>4</sub> (A, B = Co, Ni, Zn, Mn, Fe, etc.), typically in a spinel structure. Sun *et al.*<sup>13</sup> and Lou *et al.*<sup>15</sup> reviewed the most common MTMOs in their literature, such as NiCo<sub>2</sub>O<sub>4</sub>,<sup>16</sup> ZnCo<sub>2</sub>O<sub>4</sub>,<sup>17</sup> ZnMn<sub>2</sub>O<sub>4</sub>,<sup>18</sup> CoMn<sub>2</sub>O<sub>4</sub>,<sup>19</sup> CoFe<sub>2</sub>O<sub>4</sub>,<sup>20</sup> ZnFe<sub>2</sub>O<sub>4</sub>.<sup>21</sup>

CoMn<sub>2</sub>O<sub>4</sub>, with a high Mn proportion, is becoming one of the most potential anode and has attracted the attention of researchers due to its not only high capacity but also suitable discharge plateau (~0.6 V) as well as low cost.<sup>22</sup> Just like TMOs, MTMOs also share the disadvantage of large volume changes, agglomeration, pulverization and poor electronic conductivity to some extent. Nanostructuring and coating to form hybrid materials are two common approaches to address these challenges.<sup>1,23</sup> In the case of CoMn<sub>2</sub>O<sub>4</sub> (CMO), numerous nanostructure, such as nanowires,<sup>24</sup> nanofibers,<sup>25</sup> nanorods,<sup>26</sup> porous sphere,<sup>27</sup> hollow spheres<sup>28</sup> as well as its composite with graphene<sup>29,30</sup> have been studied by many researchers and good electrochemical performance has been achieved. Coating to form a buffering matrix is always another effective method to

<sup>a</sup>Guang Zhou Key Laboratory of Energy Materials Surface Chemistry, New Energy Research Institute, School of Environment and Energy, South China University of Technology, Guangzhou, 510006, China. E-mail: escheng@scut.edu.cn; Tel: +86-020-39380525

<sup>b</sup>School of Materials Science and Engineering, Georgia Institute of Technology, Atlanta, GA 30332-0245, USA. E-mail: meilin.liu@mse.gatech.edu; Tel: +1-404-894-6114



relieve the rapid fading capacity during charge–discharge processes.  $\text{TiO}_2$  is considered a suitable zero-strain shell for application in LIBs anodes. Its fascinating features, such as plentiful polymorphs, good chemical and thermal stability, excellent electronic and optical properties render it greatly promising not only in photocatalysis, solar cells but also in LIBs.<sup>31</sup> Various  $\text{TiO}_2$  with different structure and morphology have been synthesized and investigated as anodes in LIBs. For example, porous  $\text{TiO}_2$  spheres composed of interconnected nanorods<sup>32</sup> and porous  $\text{TiO}_2$  urchins constructed from connected nanocrystals<sup>33</sup> have ever been studied and hierarchical structured  $\text{TiO}_2$  showed better performance than commercial  $\text{TiO}_2$ . In addition, great effort has been directed toward synthesis of core@ $\text{TiO}_2$  structures. For example, Wang *et al.*<sup>34</sup> fabricated  $\text{SnO}_2$ @ $\text{TiO}_2$  core–shell structure as anode materials for LIBs, which displayed excellent electrochemical performance. Zhao *et al.*<sup>35</sup> successfully constructed core–shell  $\alpha\text{-Fe}_2\text{-O}_3$ @ $\text{TiO}_2$  microellipsoids and studied the formation mechanisms in detail. Kim *et al.*<sup>36</sup> synthesized  $\text{SiO}_2$ @ $\text{TiO}_2$  spherical core–shell particles and they presented good catalytic performance in decomposing methyl orange. So far, no literature has reported  $\text{TiO}_2$  coated CMO as anode materials for LIBs.

In this work, a simple solvothermal approach was designed for the synthesis of carbonate precursors of CMO. After the carbonate precursors were calcined in air at 600 °C for 3 h, uniform porous CMO spheres with high yields were obtained. Surprisingly, the porous CMO spheres with diameters of 600–800 nm consist of numerous polyhedral nanoparticles. The obtained CMO was further used as the original material to synthesize the CMO@ $\text{TiO}_2$  core–shell structure through a hydrolysis and condensation process using tetrabutyl titanate (TBOT) as the titanium source and the ammonia as the catalyst. The as-obtained porous CMO@ $\text{TiO}_2$  spheres exhibit good cycling and rate performance when utilized as anode materials. The first discharge capacities of CMO and CMO@ $\text{TiO}_2$  are 959 and 1100 mA h g<sup>−1</sup>, respectively, showing an initial efficiencies of 70.4% and 67.6%, respectively. After cycling at a current density of 1000 mA g<sup>−1</sup> for 500 cycles, the specific capacity of CMO@ $\text{TiO}_2$  was stabilized at around 940 mA h g<sup>−1</sup>, much higher than pristine CMO.

## 2. Experimental procedure

### 2.1. Sample synthesis

All the reagents used were supplied by Damao Chemical Reagent Factory (Tianjin, China) of analytical grade and used without any further purification.

**Synthesis of CMO porous submicrospheres.** Typically, 0.5 mmol  $\text{Co}(\text{CH}_3\text{COO})_2 \cdot 4\text{H}_2\text{O}$ , 1 mmol  $\text{Mn}(\text{CH}_3\text{COO})_2 \cdot 4\text{H}_2\text{O}$  and 30 mmol  $\text{NH}_4\text{HCO}_3$  were dissolved in 60 mL of ethylene glycol (EG) under stirring. After stirring for 1 h, the transparent solution was transferred into a 100 mL Teflon-lined stainless steel autoclave and maintained at 200 °C for 20 h. After the autoclave was cooled naturally to room temperature, samples depositing at the bottom were collected and washed by centrifugation for several times using deionized water and absolute ethanol. The as-synthesized samples were then dried in

a vacuum oven at 80 °C overnight to get pink powders as precursor. To obtain CMO porous spheres, the precursor was calcined at 600 °C for 3 hours in air at a heating rate of 2 °C min<sup>−1</sup> to form dark green powder.

**Synthesis of CMO@ $\text{TiO}_2$  submicrospheres.** 100 mg CMO powders were dispersed in 100 mL absolute ethanol mixed with 0.3 mL ammonia solution (25 wt%) under ultrasound for 30 min. Afterward, 1 mL tetrabutyl titanate (TBOT) was added dropwise into the above solution using injector (1 mL) under stirring and the reaction was allowed to proceed for 24 h at 45 °C under continuous magnetic stirring. The resultant products were collected and washed by centrifugation with deionized water and absolute ethanol for 3 times, respectively. Then, the obtained powders were dried at 80 °C overnight. Finally, the resulting samples were calcined at 500 °C in air for 2 h at a heating rate of 3 °C min<sup>−1</sup> to remove the organic species and improve crystallinity.

### 2.2. Characterizations

X-ray diffraction (XRD) patterns were recorded on a Bruker D8 advance X-ray diffractometer using Cu K $\alpha$  radiation ( $\lambda = 0.15406$  nm). X-ray photoelectron spectroscopy (XPS) measurements were performed on a PHI Quantera II instrument with Al K $\alpha$  radiation. Scanning electron microscopy (SEM) images were obtained using a field emission scanning electron microscope (FE-SEM, Hitachi LEO 1530). Transmission electron microscopy (TEM) and high-resolution TEM (HRTEM) were taken on a JEM-2100F.

### 2.3. Electrochemical measurements

Electrochemical measurements were performed at 25 °C in thermostat using CR 2025-type coin cells with Celgard 2400 porous polypropylene membrane as separator, lithium-foil as both counter electrode and reference electrode and 1 M LiPF<sub>6</sub> in EC/DMC (1 : 1 by volume) as electrolyte. The working electrode was prepared by making a slurry of active materials, acetylene black (AB), and polyvinylidene difluoride (PVDF) in a weight ratio of powder/AB/PVDF = 7 : 2 : 1 in *N*-methylpyrrolidone (NMP) onto a copper foil current collector and then drying at 80 °C under vacuum for 10 h, and a mass loading of the active materials was about 0.45–0.5 mg cm<sup>−2</sup>. The cells were assembled in an Ar-filled glovebox with moisture and oxygen contents both below 0.1 ppm. The cycling and rate performance tests of the samples were performed on a Land battery test system (CT2001A). The cyclic voltammetry (CV) was tested in the voltage of 0.01 to 3.0 V at a scan rate of 0.1 mV s<sup>−1</sup> by an electrochemical workstation (CHI660E).

## 3. Results and discussion

### 3.1. Structure and morphology characterization

The synthesis process of porous CMO@ $\text{TiO}_2$  submicrospheres is depicted in Fig. 1. Pink carbonate precursor is first synthesized through a solvothermal process with assistant of  $\text{NH}_4\text{HCO}_3$ . The precursor is then calcined under air to form porous CMO submicrospheres which can be ascribed to the



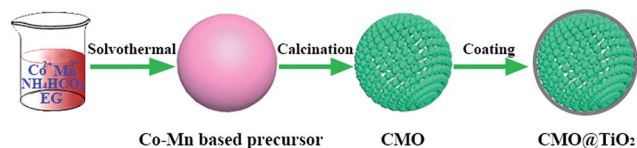


Fig. 1 Schematic illustration of the growth of porous CMO@TiO<sub>2</sub> submicrospheres.

escape of CO<sub>2</sub> gas from the material during the heating process. Subsequently, a thin layer of TiO<sub>2</sub> was coated on the surface of the spheres through a hydrolysis and following condensation process using TBOT as titanium source and ammonia as catalyst and a composite of CMO@TiO<sub>2</sub> with sphere morphology was finally obtained.

The chemical compositions of the samples were first characterized by X-ray diffraction (XRD) technology and presented in Fig. 2. Fig. 2a shows the XRD pattern of the carbonate precursor prepared through NH<sub>4</sub>HCO<sub>3</sub> assisted solvothermal process with the molar ratio of Co and Mn being 1 : 2. By comparison with MnCO<sub>3</sub> (JCPDS no. 85-1109), all the diffraction peaks could be indexed on the basis of the hexagonal phase with a space group  $R\bar{3}c$  (no. 167).<sup>28</sup> After calcined at 600 °C for 3 hours in air, all of the reflections could be indexed as tetragonal (Co, Mn)(Co, Mn)<sub>2</sub>O<sub>4</sub> ( $a = b = 8.09$  Å,  $c = 9.27$  Å; Co : Mn = 1 : 2; JCPDS no. 18-0408) with a spinel structure, as illustrated in Fig. 2b. No other diffraction peaks are observed, implying a high purity of the products. For the CMO@TiO<sub>2</sub> composite, the diffraction peaks agree well with the CMO except that the intensities of the peaks decrease. No clear TiO<sub>2</sub> diffraction peaks can be seen from the pattern, which may ascribe to its low content.

XPS analyses were carried out to further investigate the composition of CMO@TiO<sub>2</sub> and the valence states of its metal ions. All of the binding energies in this XPS analysis were corrected for specimen charging by referencing them to the C 1s peak (set at 284.6 eV). As shown in the survey scan of CMO@TiO<sub>2</sub> (Fig. 3a), the CMO@TiO<sub>2</sub> hybrid contains four elements (except carbon): cobalt, manganese, oxygen and titanium. In the Co 2p spectrum of Fig. 3b, peak at 781.2 eV is assigned to Co 2p<sub>3/2</sub>, while the peak at 796.9 eV is attributed to Co 2p<sub>1/2</sub>. Whereas, the two peaks are accompanied by two prominent shakeup satellite peaks (786.3 and 802.9 eV, respectively). The main peaks and satellite peaks indicate the presence of Co(II) and Co(III) cations.<sup>29,37–39</sup> It can be seen from

Fig. 3c that the Mn 2p spectrum exhibits two peaks at 641.7 and 653.3 eV which can be referred to the binding energies of the 2p<sub>3/2</sub> and 2p<sub>1/2</sub>, respectively. After refined fitting, the spectrum can be divided into four peaks. Among them, 641.5 and 653.0 eV can be assigned to the existence of Mn(II), while other two peaks at 642.9 and 653.7 eV are characteristic of Mn(III) cation.<sup>40</sup> In Fig. 3d, XPS investigation on the titanium chemical state shows two binding energy located at 458.5 eV and 464.1 eV, which can be indexed to Ti 2p<sub>3/2</sub> and Ti 2p<sub>1/2</sub>, respectively, indicating a valance state of Ti(IV).<sup>41,42</sup>

The morphology and microstructure of the carbonate precursors and corresponding CMO@TiO<sub>2</sub> were then characterized by scanning electron microscopy (SEM). As shown in Fig. 4a, the precursor is formed with well-defined spheres with an average diameter of about 800 nm. While, the spheres are composed of countless much smaller polyhedral nanoparticles and hence cause the formation of a rough surface (Fig. 4b). After calcinated in air, the carbonate particles are transformed into CMO spheres with a similar diameter but much porous structure due to the release of CO<sub>2</sub> during calcination. After coating with TiO<sub>2</sub>, the morphology is remained (Fig. 4c). From the enlarged SEM image of Fig. 4d, it can be seen that the nanoparticles that make up the spheres become larger after calcination, compared with those of the carbonate precursor, and a lot voids are formed. Besides, elemental mapping image of the porous spheres (Fig. 4e) show well matched spatial distributions of Co, Mn, O and Ti, further confirming the successful coating of TiO<sub>2</sub>, which is agreed well with the XPS analysis.

To get more detailed information about the morphology and the crystal structure of the materials, TEM and HRTEM observations were employed. It can be found from Fig. 5a that the carbonate precursors have a solid interior structure and its rough surface can be clearly seen from a higher magnification image in Fig. 5b, which is in consistent with the SEM results. CMO porous spheres are obtained by sintering the carbonate precursors at 600 °C for 3 h in air. After coating with TiO<sub>2</sub>, the porous structure is remained (Fig. 5c) and a thin layer can be seen along the edge of CMO, as indicated by the arrows in Fig. 5d. In one white oval area of the HRTEM image (Fig. 5e), distinct lattice fringes with an interplanar spacing of 0.349 nm (enlarged in the inset at the right top) can be observed, which can be attributed to the (101) plane of TiO<sub>2</sub> phase, verifying the thin coating layer is indeed TiO<sub>2</sub>.

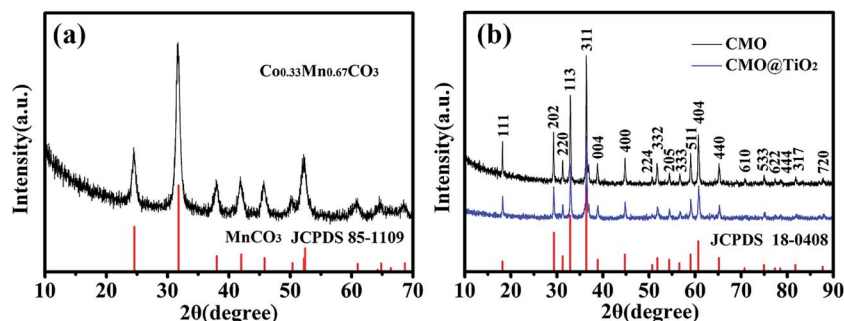


Fig. 2 XRD patterns of the (a) carbonate precursors and (b) CMO and CMO@TiO<sub>2</sub> powders.





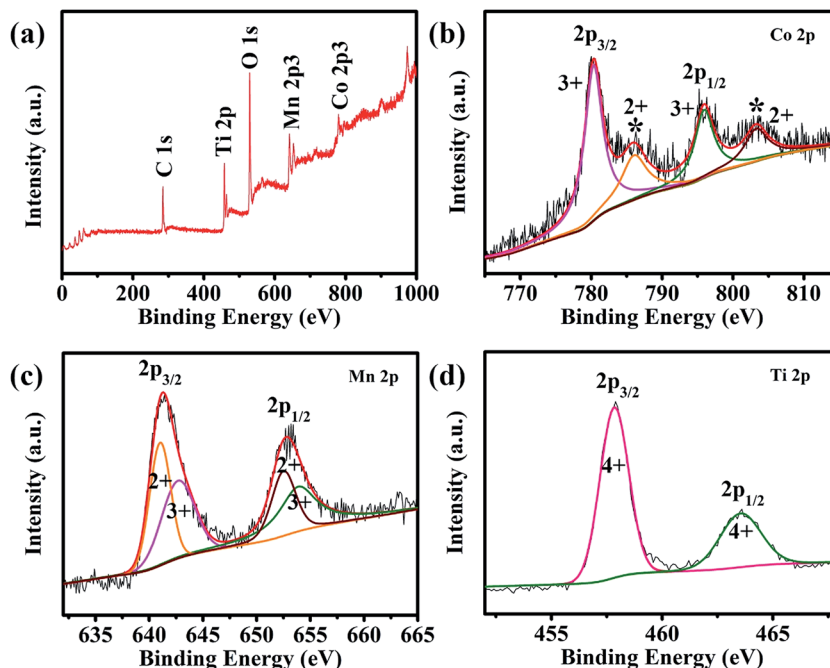


Fig. 3 XPS spectra of CMO@TiO<sub>2</sub> powders: (a) survey, (b) Co 2p, (c) Mn 2p, (d) Ti 2p, respectively.

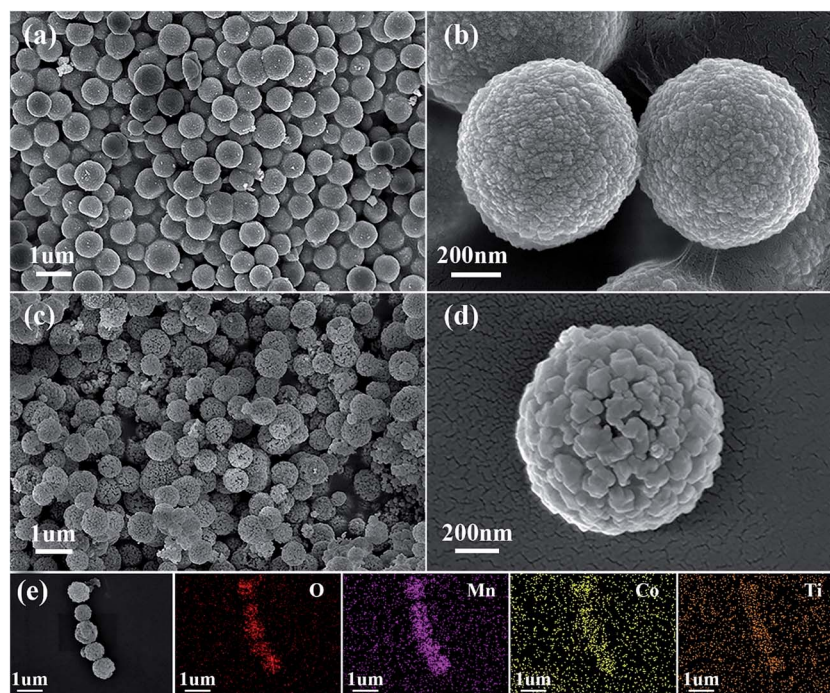


Fig. 4 SEM images of the (a and b) Co–Mn carbonate precursors, (c and d) the CMO@TiO<sub>2</sub> composite and (e) a strand of submicrospheres and the corresponding EDX elemental mappings of O, Mn, Co and Ti.

Besides, another HRTEM region standing for the core substance is marked with white square (Fig. 5e). From its enlarged image in Fig. 5f, clear lattice fringes with an interplanar distance of 0.486 nm and 0.285 nm can be observed, corresponding to the spacings of (111) and (220) planes of CMO crystals, respectively, which is agreed well with the XRD analysis.

### 3.2. Electrochemical properties

After assembled to be half-cells, electrochemical properties of the CMO@TiO<sub>2</sub> and CMO are characterized and presented in Fig. 6. Fig. 6a shows the cyclic voltammetry (CV) curves of CMO@TiO<sub>2</sub> electrodes at a scan rate of 0.1 mV s<sup>−1</sup> in a potential range 0.01–3.0 V. As can be seen, the CV curve for the first cycle



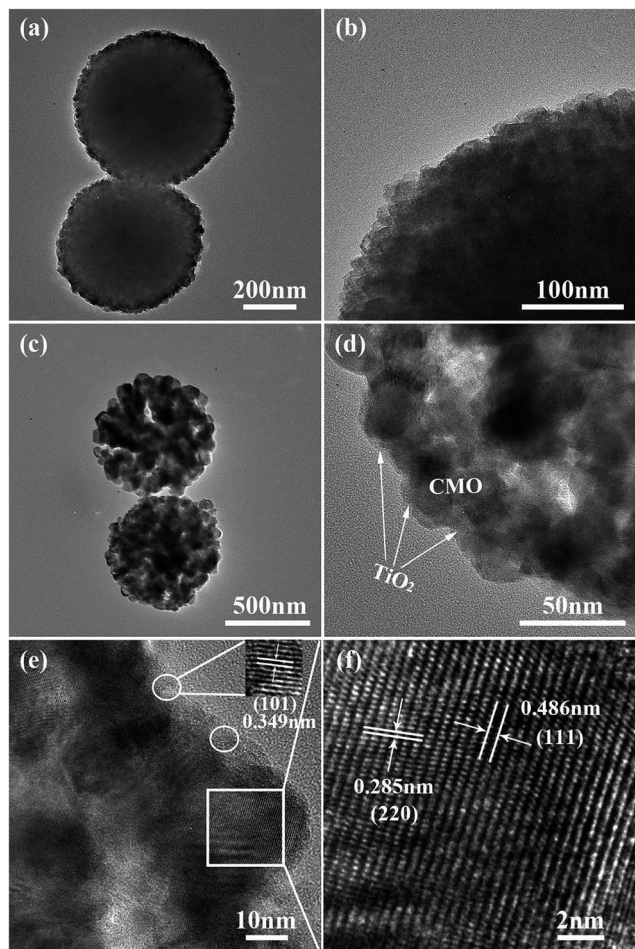
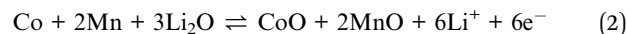
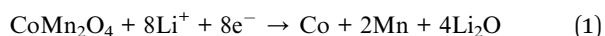


Fig. 5 (a and b) TEM images of the Co–Mn carbonate precursors and (c and d) of the CMO@TiO<sub>2</sub> porous submicrospheres, (e) HRTEM image of CMO@TiO<sub>2</sub>, (f) enlarged lattice fringes of the white square area in (e).

is obviously different from those of the subsequent ones. In the first reduction sweep, three peaks at  $\sim 1.24$  V,  $\sim 0.53$  V and  $\sim 0.77$  V can be found. The broad peak at  $\sim 1.24$  V can be assigned to the reduction of Co<sup>3+</sup> and Mn<sup>3+</sup> to Co<sup>2+</sup> and Mn<sup>2+</sup>, and the sharp peak at  $\sim 0.53$  V is attributed to the reduction of Co<sup>2+</sup> and Mn<sup>2+</sup> to metallic Co and Mn, respectively,<sup>25,43,44</sup> while the minor peak at  $\sim 0.77$  V can be ascribed to the irreversible decomposition of the solvent in the electrolyte to form the solid electrolyte interface (SEI).<sup>19,45</sup> Two broad oxidation peaks are observed at  $\sim 1.34$  and  $1.97$  V in the anodic scan, corresponding to the oxidation of Mn to Mn<sup>2+</sup> and Co to Co<sup>2+</sup>, respectively. From the second cycle onward, the repeated redox peaks at  $0.55/1.42$  V and  $1.14/2.03$  V belong to the reduction-oxidation of MnO/Mn and CoO/Co, respectively.<sup>28</sup> Furthermore, voltage gaps of the redox couples are increased at the second cycle, implying irreversible reactions and capacity fading, which should be attributed to polarization and possible agglomeration of the materials.<sup>46</sup> On the basis of the CV analysis above, the entire electrochemical process can be indicated as follows:



The discharge–charge profiles of the CMO and CMO@TiO<sub>2</sub> porous spheres at a current density of  $200 \text{ mA g}^{-1}$  for the 1<sup>st</sup>, 2<sup>nd</sup>, 3<sup>rd</sup> cycles are exhibited in Fig. 6b and c, respectively. The CMO electrode delivers initial discharge and charge capacities of  $958.9$  and  $675.1 \text{ mA h g}^{-1}$ , respectively, corresponding to a coulombic efficiency of  $70.4\%$ , while CMO@TiO<sub>2</sub> electrode gives initial discharge and charge capacities of  $1100.8$  and  $743.8 \text{ mA h g}^{-1}$  with a slight lower coulombic efficiency of  $67.5\%$ . The formation of the SEI film and partial decomposition of Li<sub>2</sub>O are likely responsible for the large irreversible capacity loss during the first cycle. Other factors, such as kinetic limitations and the intrinsic nature of the materials, may also play a part. From the second cycle onward, the coulombic efficiency increases to about  $98\%$  and retains this value for the subsequent cycles.

Rate performance of the samples were then studied at different current densities stepwise from  $200$  to  $5000 \text{ mA g}^{-1}$  with ten cycles for each step after initially activate for 2 cycles at a current density of  $100 \text{ mA g}^{-1}$  (Fig. 6d). As seen from the figure, CMO@TiO<sub>2</sub> shows better rate capability than that of CMO with average discharge capacities of  $676, 582, 459, 328$  and  $196 \text{ mA h g}^{-1}$  at  $200, 500, 1000, 2000$  and  $5000 \text{ mA g}^{-1}$ , respectively. The improved rate performance may be aroused from the nano-scaled self-building electric field and some defects at the continuous coherent heterointerfaces of the CMO and the TiO<sub>2</sub> coating layer.<sup>47–49</sup>

To further investigate the electrochemical performance of the samples before and after coating, long cycling test at a current density of  $1000 \text{ mA g}^{-1}$  for  $500$  cycles was performed and the corresponding results are exhibited in Fig. 6e. Capacities of the two samples show a similar trend that goes down in the first  $75$  cycles and then gradually increases to a certain value. For sample CMO@TiO<sub>2</sub>, it still suffer from severe structure degradation because of the volume change resulting from conversion reaction. SEI films will fracture and new active surfaces will be exposed accompanied by the growth of new SEI along with the morphology change. This can bring enormous capacity fading, especially at higher current density.<sup>46,50</sup> The subsequent capacity increase should be attributed to the high-rate lithiation induced reactivation due to the construction of new structures and optimized stable SEI.<sup>51–53</sup>

It is apparent that the CMO@TiO<sub>2</sub> electrode exhibits much improved rate and cycling capabilities, which can be ascribed to the following reasons: (1) the thin layer of TiO<sub>2</sub> as a zero-strain shell together with the porous structure can constrain the large volume change of the CMO materials to some extent and thus reduce the materials from pulverization, leading to improvement in capacity retention upon extended cycling; (2) self-building electric field and some defects, such as Ti<sub>Mn</sub>, were formed at the interface of TiO<sub>2</sub> and CMO, which can probably enhance the conductivity of CMO and hence the rate capacity.





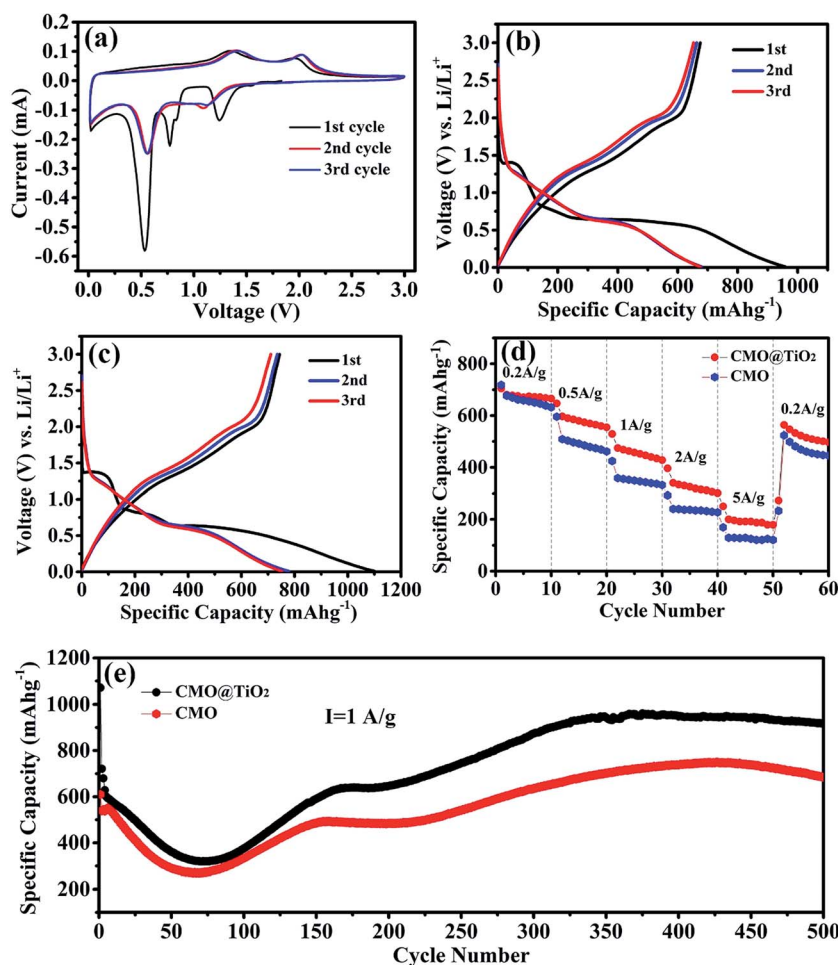


Fig. 6 (a) CV curves of the CMO@TiO<sub>2</sub> at a scan rate of 0.1 mV s<sup>-1</sup> in a voltage range of 0.01–3.00 V vs. Li<sup>+</sup>/Li; charge–discharge profiles of the (b) CMO and (c) CMO@TiO<sub>2</sub> porous submicrospheres for the 1<sup>st</sup>, 2<sup>nd</sup>, 3<sup>rd</sup> cycles at a current density of 200 mA g<sup>-1</sup>; (d) rate performance of the CMO and CMO@TiO<sub>2</sub> submicrospheres electrode; (e) cycling performance of the CMO and CMO@TiO<sub>2</sub> submicrospheres at a current density of 1 A g<sup>-1</sup>.

## 4. Conclusions

In summary, this work reports a facile method for a controllable preparation of porous CMO and CMO@TiO<sub>2</sub> spheres. When evaluated as anode materials, the CMO@TiO<sub>2</sub> exhibits better cycling and rate performance than the pristine CMO. The excellent electrochemical performance may originate from the nano-sized particles, porous structure and the thin layer coating of TiO<sub>2</sub>. As a coating layer, the zero-strain TiO<sub>2</sub> shell may effectively buffer the large volume change and prevent the materials from pulverization during the charge/discharge processes. This work shows that metal oxides coating is an effective way to improve the performance of mixed transition metal oxides, which effectively promote their potential applications as anode materials for next generation energy storage electrodes.

## Acknowledgements

This work was supported by the National Science Foundation for Young Scientists of China (no. 21403073), Fundamental Research Funds for Central Universities of SCUT, China (no.

2015ZZ118) and Guangdong Innovative and Entrepreneurial Research Team Program (2014ZT05N200).

## References

- 1 B. Zhao, R. Ran, M. L. Liu and Z. P. Shao, *Mater. Sci. Eng., R*, 2015, **98**, 1–71.
- 2 X. Han, H. X. Chen, Z. Q. Zhang, D. L. Huang, J. F. Xu, C. Li, S. Y. Chen and Y. Yang, *J. Mater. Chem. A*, 2016, **4**, 17757–17763.
- 3 H. Wu, G. Chan, J. W. Choi, I. Ryu, Y. Yao, M. T. McDowell, S. W. Lee, A. Jackson, Y. Yang, L. B. Hu and Y. Cui, *Nat. Nanotechnol.*, 2012, **7**, 310–315.
- 4 J. Y. Wang, N. L. Yang, H. J. Tang, Z. H. Dong, Q. Jin, M. Yang, D. Kisailus, H. J. Zhao, Z. Y. Tang and D. Wang, *Angew. Chem., Int. Ed.*, 2013, **52**, 6417–6420.
- 5 H. Wu, M. Xu, Y. C. Wang and G. F. Zheng, *Nano Res.*, 2013, **6**, 167–173.
- 6 Q. Guan, J. L. Cheng, B. Wang, W. Ni, G. F. Gu, X. D. Li, L. Huang, G. C. Yang and F. D. Nie, *ACS Appl. Mater. Interfaces*, 2014, **6**, 7626–7632.



- 7 S. Z. Huang, Y. Cai, J. Jin, J. Liu, Y. Li, Y. Yu, H. E. Wang, L. H. Chen and B. L. Su, *Nano Energy*, 2015, **12**, 833–844.
- 8 S. Y. Gao and K. Geng, *Nano Energy*, 2014, **6**, 44–50.
- 9 K. Z. Cao, L. F. Jiao, H. Q. Liu, Y. C. Liu, Y. J. Wang, Z. P. Guo and H. T. Yuan, *Adv. Energy Mater.*, 2015, **5**, 1401421.
- 10 W. J. Yu, L. L. Zhang, P. X. Hou, F. Li, C. Liu and H. M. Cheng, *Adv. Energy Mater.*, 2016, **6**, 1501755.
- 11 Z. Y. Fan, J. Liang, W. Yu, S. J. Ding, S. D. Cheng, G. Yang, Y. L. Wang, Y. X. Xi, K. Xi and R. V. Kumar, *Nano Energy*, 2015, **16**, 152–162.
- 12 Y. Xiao, C. W. Hu and M. H. Cao, *J. Power Sources*, 2014, **247**, 49–56.
- 13 Y. Zhao, X. F. Li, B. Yan, D. B. Xiong, D. J. Li, S. Lawes and X. L. Sun, *Adv. Energy Mater.*, 2016, **6**, 1502175.
- 14 C. T. Cherian, J. Sundaramurthy, M. V. Reddy, P. S. Kumar, K. Mani, D. Pliszka, C. H. Sow, S. Ramakrishna and B. V. R. Chowdari, *ACS Appl. Mater. Interfaces*, 2013, **5**, 9957–9963.
- 15 C. Z. Yuan, H. B. Wu, Y. Xie and X. W. Lou, *Angew. Chem., Int. Ed.*, 2014, **53**, 1488–1504.
- 16 L. F. Shen, L. Yu, X. Y. Yu, X. G. Zhang and X. W. Lou, *Angew. Chem., Int. Ed.*, 2015, **54**, 1868–1872.
- 17 Q. B. Zhang, J. X. Wang, J. C. Dong, F. Ding, X. H. Li, B. Zhang, S. H. Yang and K. L. Zhang, *Nano Energy*, 2015, **13**, 77–91.
- 18 N. N. Wang, X. J. Ma, H. Y. Xu, L. Chen, J. Yue, F. E. Niu, J. Yang and Y. T. Qian, *Nano Energy*, 2014, **6**, 193–199.
- 19 L. Zhou, D. Y. Zhao and X. W. Lou, *Adv. Mater.*, 2012, **24**, 745–748.
- 20 Y. Wang, D. W. Su, A. Ung, J. H. Ahn and G. X. Wang, *Nanotechnology*, 2012, **23**, 055402.
- 21 L. R. Hou, L. Lian, L. H. Zhang, G. Pang, C. Z. Yuan and X. G. Zhang, *Adv. Funct. Mater.*, 2015, **25**, 238–246.
- 22 L. H. Zhang, L. R. Hou, L. Lian, L. S. Wang and C. Z. Yuan, *Rare Met. Mater. Eng.*, 2016, **45**, 1910–1916.
- 23 P. G. Bruce, B. Scrosati and J. M. Tarascon, *Angew. Chem., Int. Ed.*, 2008, **47**, 2930–2946.
- 24 Y. N. Xu, X. F. Wang, C. H. An, Y. J. Wang, L. F. Jiao and H. T. Yuan, *J. Mater. Chem. A*, 2014, **2**, 16480–16488.
- 25 G. R. Yang, X. Xu, W. Yan, H. H. Yang and S. J. Ding, *Electrochim. Acta*, 2014, **137**, 462–469.
- 26 L. J. Wang, B. Liu, S. H. Ran, L. M. Wang, L. N. Gao, F. Y. Qu, D. Chen and G. Z. Shen, *J. Mater. Chem. A*, 2013, **1**, 2139–2143.
- 27 L. Hu, H. Zhong, X. R. Zheng, Y. M. Huang, P. Zhang and Q. W. Chen, *Sci. Rep.*, 2012, **2**, 986.
- 28 J. F. Li, S. L. Xiong, X. W. Li and Y. T. Qian, *Nanoscale*, 2013, **5**, 2045–2054.
- 29 Y. S. Liu, J. Li, W. Z. Li, Y. M. Li, Q. Y. Chen and F. Q. Zhan, *J. Power Sources*, 2015, **299**, 492–500.
- 30 G. X. Gao, S. Y. Lu, Y. Xiang, B. T. Dong, W. Yan and S. J. Ding, *Dalton Trans.*, 2015, **44**, 18737–18742.
- 31 X. Chen and S. S. Mao, *Chem. Rev.*, 2007, **107**, 2891–2959.
- 32 Y. Cai, H. E. Wang, J. Jin, S. Z. Huang, Y. Yu, Y. Li, S. P. Feng and B. L. Su, *Chem. Eng. J.*, 2015, **281**, 844–851.
- 33 Y. Cai, H. E. Wang, S. Z. Huang, M. F. Yuen, H. H. Cai, C. Wang, Y. Yu, Y. Li, W. J. Zhang and B. L. Su, *Electrochim. Acta*, 2016, **210**, 206–214.
- 34 Z. Yi, Q. G. Han, P. Zan, Y. Cheng, Y. M. Wu and L. M. Wang, *J. Mater. Chem. A*, 2016, **4**, 12850–12857.
- 35 W. Li, J. P. Yang, Z. X. Wu, J. X. Wang, B. Li, S. S. Feng, Y. H. Deng, F. Zhang and D. Y. Zhao, *J. Am. Chem. Soc.*, 2012, **134**, 11864–11867.
- 36 J. W. Lee, M. R. Othman, Y. Eom, T. G. Lee, W. S. Kim and J. Kim, *Microporous Mesoporous Mater.*, 2008, **116**, 561–568.
- 37 S. A. Needham, G. X. Wang, K. Konstantinov, Y. Tournayre, Z. Lao and H. K. Liu, *Electrochem. Solid-State Lett.*, 2006, **9**, A315–A319.
- 38 S. L. Xiong, J. S. Chen, X. W. Lou and H. C. Zeng, *Adv. Funct. Mater.*, 2012, **22**, 861–871.
- 39 L. Liu, H. J. Zhang, J. Yang, Y. P. Mu and Y. Wang, *J. Mater. Chem. A*, 2015, **3**, 22393–22403.
- 40 L. H. Zhang, S. Q. Zhu, H. Cao, L. R. Hou and C. Z. Yuan, *Chem.–Eur. J.*, 2015, **21**, 10771–10777.
- 41 M. Sathish, B. Viswanathan, R. P. Viswanath and C. S. Gopinath, *Chem. Mater.*, 2005, **17**, 6349–6353.
- 42 H. G. Yang and H. C. Zeng, *J. Phys. Chem. B*, 2004, **108**, 3492–3495.
- 43 M. H. Kim, Y. J. Hong and Y. C. Kang, *RSC Adv.*, 2013, **3**, 13110–13114.
- 44 Y. R. Liu, B. C. Zhang, J. K. Feng and S. L. Xiong, *RSC Adv.*, 2015, **5**, 26863–26871.
- 45 L. X. Zhang, G. F. He, S. W. Lei, G. S. Qi, H. F. Jiu and J. Wang, *J. Power Sources*, 2016, **326**, 505–513.
- 46 X. Zhao, J. H. Sui, F. Li, H. T. Fang, H. G. Wang, J. Y. Li, W. Cai and G. Z. Cao, *Nanoscale*, 2016, **8**, 17902–17910.
- 47 Y. Cai, H. E. Wang, X. Zhao, F. Huang, C. Wang, Z. Deng, Y. Li, G. Z. Cao and B. L. Su, *ACS Appl. Mater. Interfaces*, 2017, **9**, 10652–10663.
- 48 T. F. Zhou, Y. Zheng, H. Gao, S. D. Min, S. Li, H. K. Liu and Z. P. Guo, *Adv. Sci.*, 2015, **2**, 1500027.
- 49 H. T. Fang, M. Liu, D. W. Wang, T. Sun, D. S. Guan, F. Li, J. Zhou, T. K. Sham and H. M. Cheng, *Nanotechnology*, 2009, **20**, 225701.
- 50 G. D. Li, L. Q. Xu, Y. J. Zhai and Y. P. Hou, *J. Mater. Chem. A*, 2015, **3**, 14298–14306.
- 51 Y. Z. Jiang, D. Zhang, Y. Li, T. Z. Yuan, N. Bahlawane, C. Liang, W. P. Sun, Y. H. Lu and M. Yan, *Nano Energy*, 2014, **4**, 23–30.
- 52 H. T. Sun, G. Q. Xin, T. Hu, M. P. Yu, D. Shao, X. Sun and J. Lian, *Nat. Commun.*, 2014, **5**, 1.
- 53 M. H. Chen, J. L. Liu, D. L. Chao, J. Wang, J. H. Yin, J. Y. Lin, H. J. Fan and Z. X. Shen, *Nano Energy*, 2014, **9**, 364–372.

